



Three-dimensional FEM derived elastic Green's functions for the coseismic deformation of the 2005 M_w 8.7 Nias-Simeulue, Sumatra earthquake

Ya-Ju Hsu

Institute of Earth Sciences, Academia Sinica, 28 Academia Road, Section 2, Nankang, Taipei 115, Taiwan (yaru@earth.sinica.edu.tw)

Mark Simons

Division of Geological and Planetary Sciences, California Institute of Technology, Pasadena, California 91125, USA

Charles Williams

GNS Science, Lower Hutt 5040, New Zealand

Emanuele Casarotti

Istituto Nazionale di Geofisica e Vulcanologia, Via di Vigna Murata, I-00143 Rome, Italy

[1] Using finite element models (FEMs), we examine the sensitivity of surface displacements to the location of fault slip, topography, and three-dimensional variations in elastic moduli in the context of a 2-D infinite thrust fault. We then evaluate the impact of these factors and fault geometry on surface displacements and estimates of the distribution of coseismic slip associated with the 2005 M_w 8.7 Nias-Simeulue, Sumatra earthquake. Topographic effects can be significant near the trench, where bathymetric gradients are highest and the fault is closest to the free surface. Variations in Young's modulus can significantly alter predicted deformation. Surface displacements are relatively insensitive to perturbations in Poisson's ratio for shear sources, but may play a stronger role when the source has a dilatational component. If we generate synthetic displacements using a heterogeneous elastic model and then use an elastic half-space or layered earth model to estimate the slip distribution and fault geometry, we find systematic residuals of surface displacements and different slip patterns compared to the input fault slip model. The coseismic slip distributions of the 2005 earthquake derived from the same fault geometry and different material models show that the rupture areas are narrower in all tested heterogeneous elastic models compared to that obtained using half-space models. This difference can be understood by the tendency to infer additional sources in elastic half-space models to account for effects that are intrinsically due to the presence of rheological gradients. Although the fit to surface observations in our preferred 3-D FEM model is similar to that from a simple half-space model, the resulting slip distribution may be a more accurate reflection the true fault slip behavior.

Components: 8500 words, 10 figures, 3 tables.

Keywords: Green's functions; coseismic deformation; finite element model.

Index Terms: 1242 Geodesy and Gravity: Seismic cycle related deformations (6924, 7209, 7223, 7230); 8159 Tectonophysics: Rheology: crust and lithosphere (8031); 8170 Tectonophysics: Subduction zone processes (1031, 3060, 3613, 8413).



Received 7 February 2011; Revised 31 May 2011; Accepted 31 May 2011; Published 20 July 2011.

Hsu, Y.-J., M. Simons, C. Williams, and E. Casarotti (2011), Three-dimensional FEM derived elastic Green's functions for the coseismic deformation of the 2005 M_w 8.7 Nias-Simeulue, Sumatra earthquake, *Geochem. Geophys. Geosyst.*, 12, Q07013, doi:10.1029/2011GC003553.

1. Introduction

[2] Space-based geodetic techniques including Global Positioning System (GPS) and Interferometric Synthetic Aperture Radar (InSAR) now provide observations of crustal deformation with unprecedented spatial coverage. This increase in observation quantity and quality motivates a reappraisal of standard modeling assumptions. A common approach to modeling different phases of the earthquake cycle relies on the use of simple elastic dislocation modeling, where one commonly assumes that the earth can be modeled locally as either an elastic half-space [Okada, 1985, 1992] or a horizontally layered elastic half-space [e.g., Singh, 1970; Rundle, 1980; Savage, 1998]. This approach frequently results in models that match observations reasonably well, while also being computationally simple due to the semianalytic nature of elastic Green's functions describing the response at any point on the surface to a unit of slip at a given location for these one-dimensional elastic structures. Numerous studies using elastic or layered half-space dislocation models have successfully explained how accumulated elastic strain released in major fault zones and produced reasonable fits to the surface displacements [e.g., Savage, 1983; Reilinger et al., 2000; Yu et al., 2001; Simons et al., 2002; Hsu et al., 2003].

[3] However, in many geologic environments, we may have sufficient constraints on the elastic structure to warrant consideration of models that are more complex than the Poissonian layered half-space commonly adopted. Even if the resulting models fit observations no better than those using 1-D elastic structures, the resulting slip models may reflect the true fault behavior with more fidelity. For instance, finite fault source inversions based on seismic and geodetic data show that inaccurate Green's functions (elastic half-space or 1-D layered approximations) not only introduce errors into the source rupture complexity, but also limit the recovery of the slip pattern due to the blurring from increased smoothing [Graves and Wald, 2001; Wald and Graves, 2001]. In the

1989 Kalapana, Hawaii earthquake, the focal depth determined by seismic studies is 5 km deeper than that inferred from geodetic data [Du et al., 1994]. The authors conclude that the discrepancy is possibly associated with variations of elastic modulus. The study of the coseismic deformation of the 1992 Hector Mine, California earthquake shows that the main effect of the rigidity stratification is to increase the magnitude of inferred slip at depth by about 20% to 30% [Simons et al., 2002]. Similarly, comparisons of the modeling results of the 1999 Izmit, Turkey earthquake using elastic half-space and layered earth models indicate that the Coulomb stress changes at depth, the recovered centroid depth and the seismic potency are larger in a layered earth model relative to those in a uniform half-space model [Hearn and Burgmann, 2005]. Previous works demonstrated the extent to which predicted surface displacements are sensitive to assumptions of material homogeneity, elastic isotropy, and Poisson solid for subduction earthquakes [e.g., Masterlark et al., 2001; Masterlark, 2003; Masterlark and Hughes, 2008]. Their results are generally consistent with those that consider the impact of material heterogeneity on geodetic analysis of the Japan subduction zone [Sato et al., 2007]. Sato et al. [2007] also find that Young's modulus affects surface displacements more than Poisson's ratio. In California, interseismic velocities are asymmetric across the San Andreas Fault, which can also be attributed to the effects of lateral variations of crustal rigidity [Fialko, 2006]. Generally, analysis of the effect of material heterogeneity in surface deformation is probably best explored in the context of deformation associated with large earthquakes, given the high signal-to-noise ratio.

[4] Previous studies have also shown that irregular surface topography has significant effects on surface displacements and source location when the rupture source and the topography are in phase or the source is shallow [McTigue and Segall, 1988; Huang and Yeh, 1997; Williams and Wadge, 1998]. For subduction zone earthquakes, topography generally has a small influence on the surface displacement and fault slip distribution [Masterlark,



2003] because the rupture sources are usually deep compared to the surface topography. However, the topographic effect could be significant in some cases and the accuracy of modern geodetic techniques is sufficient to detect this discrepancy. We should consider this effect in the coseismic deformation modeling.

[5] As opposed to previous studies of modeling deformation of a specified earthquake with a finite element approach and different material parameters, we first examine the sensitivity of the location of fault slip, topography, and three-dimensional variations in elastic moduli on surface displacements using a 2-D infinite fault. We use this simple model to demonstrate how inversions for earthquake slip parameters may be significantly biased when the material gradients and strain are large and the material gradients are not sufficiently well represented in the model. We also show that the influence of Young's modulus on surface deformation may be larger than that of Poisson's ratio for mode II or mode III behavior associated with faulting, while Poisson's ratio may play a more important role compared to Young's modulus if the rupture source is dilatational. We then consider the impacts of topography, Poisson's ratio, and elastic heterogeneity on inferences of coseismic slip distributions and surface displacements for the specific case of the 2005 M_w 8.7 Nias-Simeulue, Sumatra earthquake. This earthquake occurred offshore Sumatra and ruptured the megathrust in the Sunda subduction zone (Figure 1a) where the plate convergence between the Indian-Australian plates and the Sunda plate is about 5.7 cm/yr. This subduction zone has generated numerous large earthquakes in the past three centuries [Chlieh *et al.*, 2007], including the 2004 M_w 9.1 Sumatra-Andaman earthquake [Subarya *et al.*, 2006]. The spatial coverage of coseismic observations from coral measurements and GPS displacements for the 2005 earthquake allow us to quantify the influence of heterogeneity on inferences of coseismic deformation (Figure 1). Beyond the exploration of the role of 3-D elastic heterogeneity, we also investigate how uncertainties in the assumed fault geometry can complicate evaluating the effect of elastic heterogeneity on the inferred distribution of fault slip.

2. Method

[6] We use the finite element method (FEM) and the 3-D finite element code, PyLith v. 0.8.3 [Williams *et al.*, 2007], to compute coseismic surface displacements and Green's functions for

the 2-D and 3-D elastic models. PyLith is designed for simulating lithospheric deformation over a wide range of spatial and temporal scales (<http://www.geodynamics.org/cig/software/pylith>). In PyLith, the governing equations for the static problem are the equations of motion, the strain-displacement equations and the constitutive law for linear elasticity. We use boundary conditions with fixed displacements perpendicular to the boundary on the sidewalls and bottom of the model. Kinematic coseismic slip is implemented using a split-node technique [Melosh and Raefsky, 1981]. We have validated our FEM models by comparing predicted FEM surface displacements for uniform coseismic slip in a homogeneous material model for the 2005 earthquake against those predicted by the analytical solution of Okada [1985]. Maximum differences in predicted surface displacement from these two approaches are typically less than 2%. Note that the Green's functions generated by PyLith (tapered slip distribution on a linear element) cannot exactly match the Okada slip (uniform slip on a square fault patch). One has to find a slip patch with the same potency as the Okada slip patch, but the slip patch in FEM will have a tapered slip distribution and lead to differences relative to the Okada solutions for shallow displacements near the slip patch [Lohman, 2007].

2.1. Two-Dimensional Model Setup

[7] We require an assumed geologic structure, from which we generate a finite element mesh. In our case, we develop a simplified 2-D plane strain conceptual model for testing purposes. We construct the necessary meshes using the CUBIT Geometry and Mesh Generation Toolkit (<http://cubit.sandia.gov>). The topography of the 2-D FEM model is a step function with elevations equal to 0 and 2 km at distances less than and greater than 200 km, respectively. The mesh resolution decreases with increasing distance from the origin. The model extends 1200 km eastward and westward from the center and 1000 km downward (Figure 2a).

2.2. Three-Dimensional Model Setup

[8] The 3-D model approximates topographic relief and bathymetry using a global digital elevation model with a horizontal grid of 30 arc seconds [Sandwell and Smith, 1997]. We interpolate the elevation with grid spacing of 5 km in the near field of the 2005 coseismic rupture and gradually increase the grid size to 100 km in the far field. The

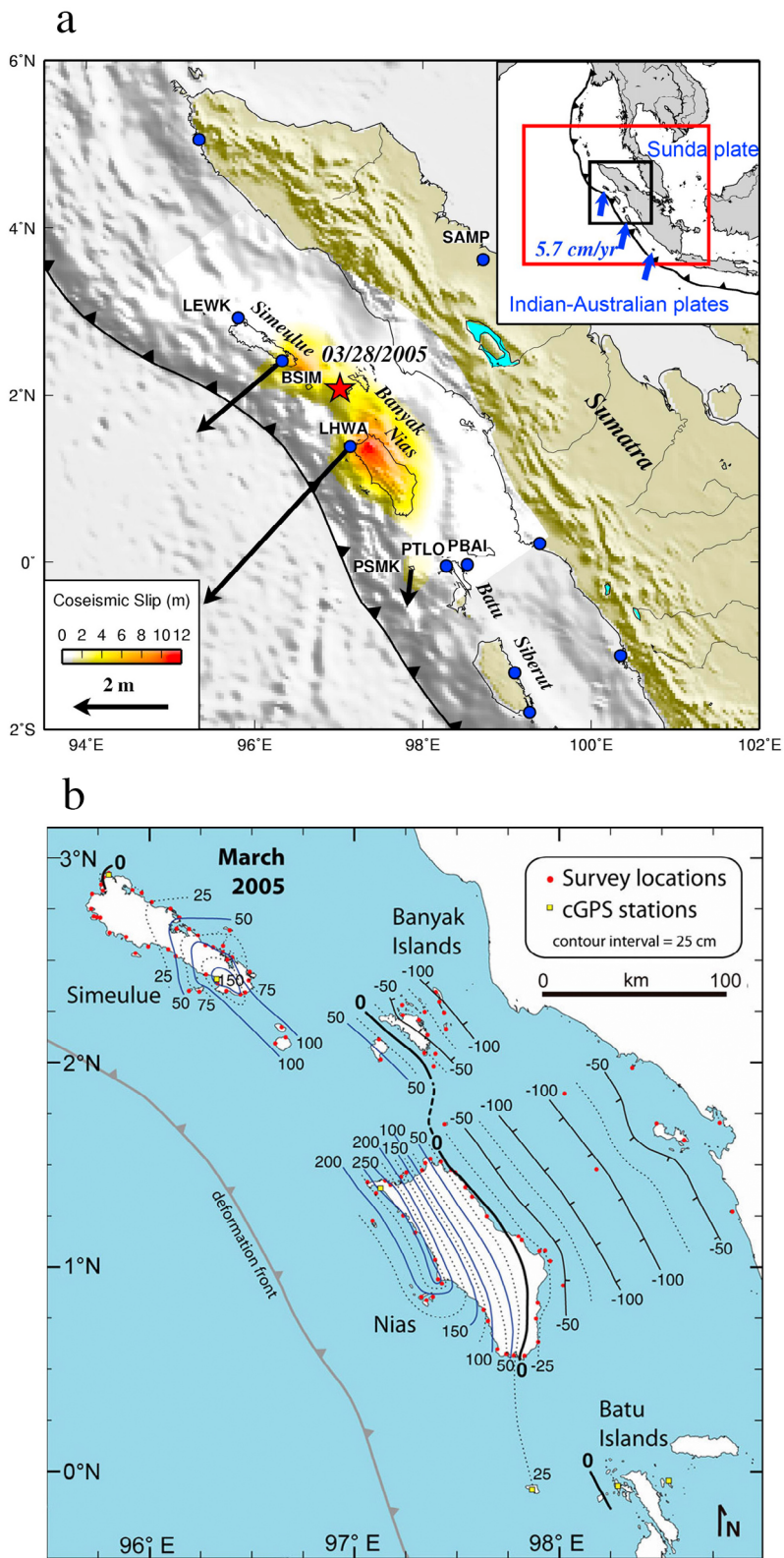


Figure 1

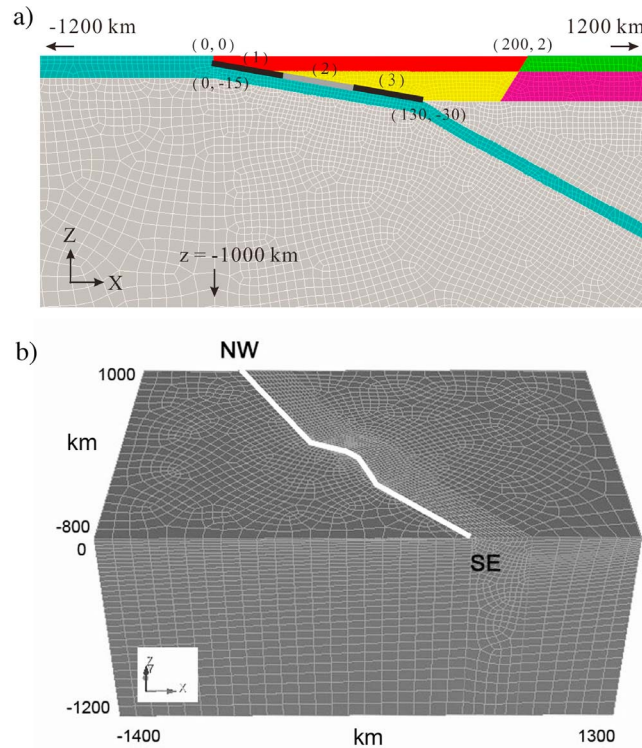


Figure 2. FEM mesh configuration. (a) Two-dimensional infinite subduction thrust fault. The fault extends 1200 km away from the origin and 1000 km at depth. The elevation is 0 km and 2 km to the west and to the east of $x = 200$ km, respectively. Color blocks indicate different material properties shown in Figure 4a and Table 1. Three rupture models (1)~(3) are used to calculate surface displacements in Figure 5. (b) Three-dimensional mesh for Sumatra with a dimension of 2700 km (length) \times 1800 km (width) \times 1200 km (height). The white line approximates the Sunda trench.

dimensions of the model are 2700 km \times 1800 km \times 1200 km in length, width, and height, respectively (Figure 2b). The top surface corresponds to real topography. Assuming the 2005 earthquake ruptured the plate interface between the Sunda plate and the Indian-Australian plates, we use a cubic spline representation to describe the fault geometry (fault *B* in Figure 3) as opposed to the kinked fault adopted in the work by *Hsu et al.* [2006] (Figure 3). The dip of the modeled fault increases from 5° at the trench top to 30° at 100 km depth (fault *B*, Figure 3). Constraints on the dip angle of the shallower por-

tion come from the joint analysis of coseismic geodetic and seismic data [*Hsu et al.*, 2006]. The bottom of the model fault is defined by relocated seismicity in this region over the past few decades [*Engdahl et al.*, 2007]. The fault plane is discretized using a total of 504 split nodes (28 and 18 nodes in the along-strike and downdip directions, respectively) on the plate interface. We partition our model into six regions with potentially different density and Young's modulus (Table 1 and Figure 4a), with values chosen in accordance to data from seismic refractions in the Sunda trench and nearby fore-arc

Figure 1. Regional map and coseismic displacement of the 2005 Nias-Simeulue, Sumatra earthquake. (a) Horizontal coseismic displacements are shown as black vectors. Color scale indicates coseismic slip distribution [*Hsu et al.*, 2006] projected to the surface. Blue dots and red star denote CGPS sites and epicenter, respectively. The black barbed line indicates the Sunda megathrust. Inset shows the regional map with motions of the Indian and Australian plates relative to the Sunda plate indicated by blue vectors. The red box indicates the region of finite element modeling. (b) Coseismic vertical displacements of the 2005 Nias-Simeulue earthquake derived from coral (red dot) and CGPS (yellow square) sites are shown in contours at 50 cm (solid line) and 25 cm (dash line) intervals. Black and blue contours indicate subsidence and uplift, respectively [*Briggs et al.*, 2006].

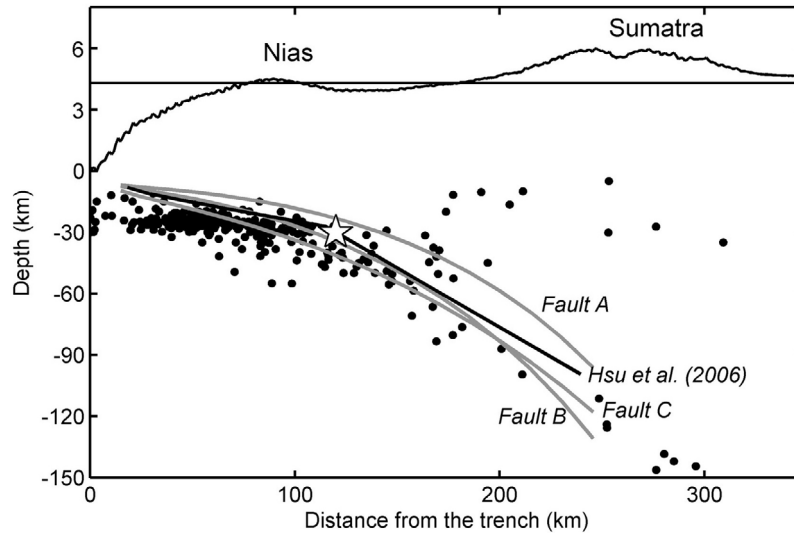


Figure 3. A 50 km wide, trench-perpendicular transect across the Nias Island and the Sumatra region. The circles denote the seismicity between 1964 and 2005 [Engdahl et al., 2007]. Grey lines indicate modeling curved faults used in finite element models. The black line denotes the fault geometry used in the work by Hsu et al. [2006]. The star is the hypocenter of the 2005 earthquake.

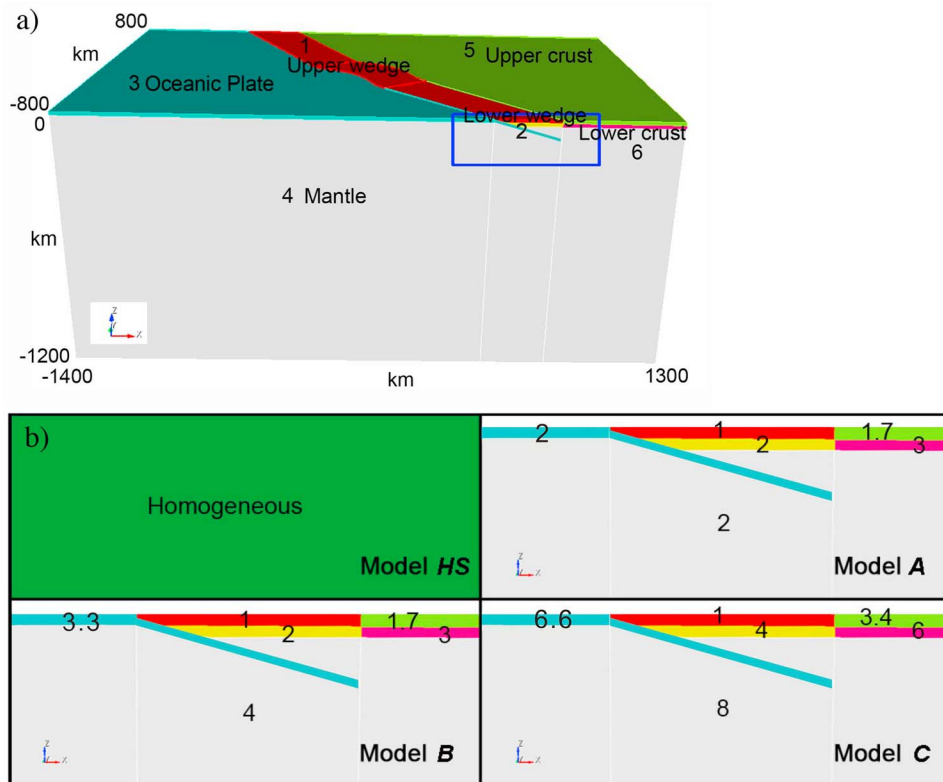


Figure 4. (a) A simplified heterogeneous elastic model in the Sumatra region. Six material properties (Table 1) are represented by different color blocks. The 3-D topographic relief is included in the model. (b) Magnified view of the blue box in Figure 4a. Numbers indicate ratios of Young's modulus (E/E_{min}). Four elastic models are tested in this study.



Table 1. The Preferable Material Model Constrained by Data From Seismic Refractions in the Sunda Trench and Nearby Fore-Arc Basins^a

ID	Material	V_p (km/s)	Density (cm ³ /g)	ν	G ($\times 10^{10}$ Pa)	E ($\times 10^{10}$ Pa)	Ratio (E/E_{\min})
1	Upper wedge	4.8	2.5	0.25	1.92	4.80	1.0
2	Lower wedge	6.6	2.7	0.25	3.92	9.80	2.0
3	Oceanic plate	8.0 ^b	3.0	0.25	6.40	16.00	3.3
4	Mantle	8.2	3.4	0.25	7.62	19.05	4.0
5	Upper crust	6.1	2.7	0.25	3.35	8.37	1.7
6	Lower crust	7.5	3.1	0.25	5.81	14.53	3.0

^aKieckhefer *et al.* [1980, 1981]. The index for each block is shown in Figure 4a with a magnified view in Figure 4b (model *B*). Abbreviations: V_p , P wave velocity; ν , Poisson's ratio; G , shear modulus; E , Young's modulus; (E/E_{\min}), the ratio of Young's modulus to the minimum value.

^bNote that the V_p of 8.0 km/s may be too high for oceanic plate. If we use a value of V_p of 6.5 km/s for oceanic plate the resulting E (8.45×10^{10} Pa) is about half of its current value (16×10^{10} Pa), while our FEM tests with $E = 8.45 \times 10^{10}$ Pa for oceanic plate show insignificant influences on the conclusions related to this change.

basins [Kieckhefer *et al.*, 1980, 1981]. These blocks are meshed using hexahedral elements. The rupture area of the 2005 earthquake is divided into small hexahedra with a size of about $3.5 \text{ km} \times 3.5 \text{ km} \times 1 \text{ km}$, grading to a larger element size of $100 \text{ km} \times 100 \text{ km} \times 2 \text{ km}$ in the far field. The final FEM model consists of 68412 nodes and 64662 elements (Figure 2b).

3. Sensitivity of Source Locations to Topography, Poisson's Ratio, and Material Properties on Surface Displacements of Infinite 2-D Dipping Thrust Fault

[9] We examine the sensitivity of source locations to variations of topography, Poisson's ratio, and material properties using a simplified 2-D plane strain model (Figure 2a). We use three different rupture models with unit dip slip applied to segments with depth ranges between 10 and 20 km, 20 and 30 km, and 30 and 40 km, respectively ((1)–(3) in Figure 2a). Two topographic models, including a flat top surface and a step function change of topography on the surface, are used to calculate surface displacements resulting from the

three rupture sources (Figures 5a and 5b). The effect of topography on surface displacements is significant above the rupture zone and when the fault is closest to the free surface (Figures 5a and 5b). Because the primary change of surface topography is far from the rupture source, the differences of vertical displacements between two topographic models are small (Figure 5b). The influence of topography on vertical displacements is less than that in horizontal displacements. Additionally, we calculate surface coseismic displacements with Poisson's ratio of 0.25 and 0.3, respectively. The results show that the difference between these two models is very small (Figures 5c and 5d). Surface displacements are not very sensitive to perturbations in Poisson's ratio in substrata.

[10] We also test the sensitivity between source locations and Young's modulus. We estimate surface displacements of different rupture sources using two material models including a uniform and a heterogeneous elastic model (model *B*, Figure 4b). The surface displacements computed from a shallow rupture source and a heterogeneous elastic model are very different from those in a homogeneous model (Figures 5e and 5f) because of distinct changes of Young's modulus at the depth range less than 30 km (Figure 2a). However, vertical

Figure 5. Profiles of surface displacements perpendicular to the trench from three rupture models ((1)–(3) in Figure 2a). From top to bottom, the ruptures with unit dip slip occur at depth ranges between 10 and 20 km (patch 1), 20 and 30 km (patch 2), and 30 and 40 km (patch 3), respectively. Grey flat bars indicate rupture zones projected to the surface. The black numbers in panels show the offsets of displacements in these plots. (a) Surface displacements perpendicular to the trench estimated from a homogeneous flat earth model (black) and a homogeneous model with surface relief (red) and the difference between them (blue). (b) Similar to Figure 5a but for vertical displacements. (c) Surface displacements perpendicular to the trench estimated from models with Poisson's ratio of 0.25 (black) and of 0.3 (red) and the difference between them (blue). (d) Similar to Figure 5c but for vertical displacements. (e) Surface displacements perpendicular to the trench estimated from a homogeneous (black) and a heterogeneous elastic (red) models and the difference between them (blue). (f) Similar to Figure 5e but for vertical displacements.

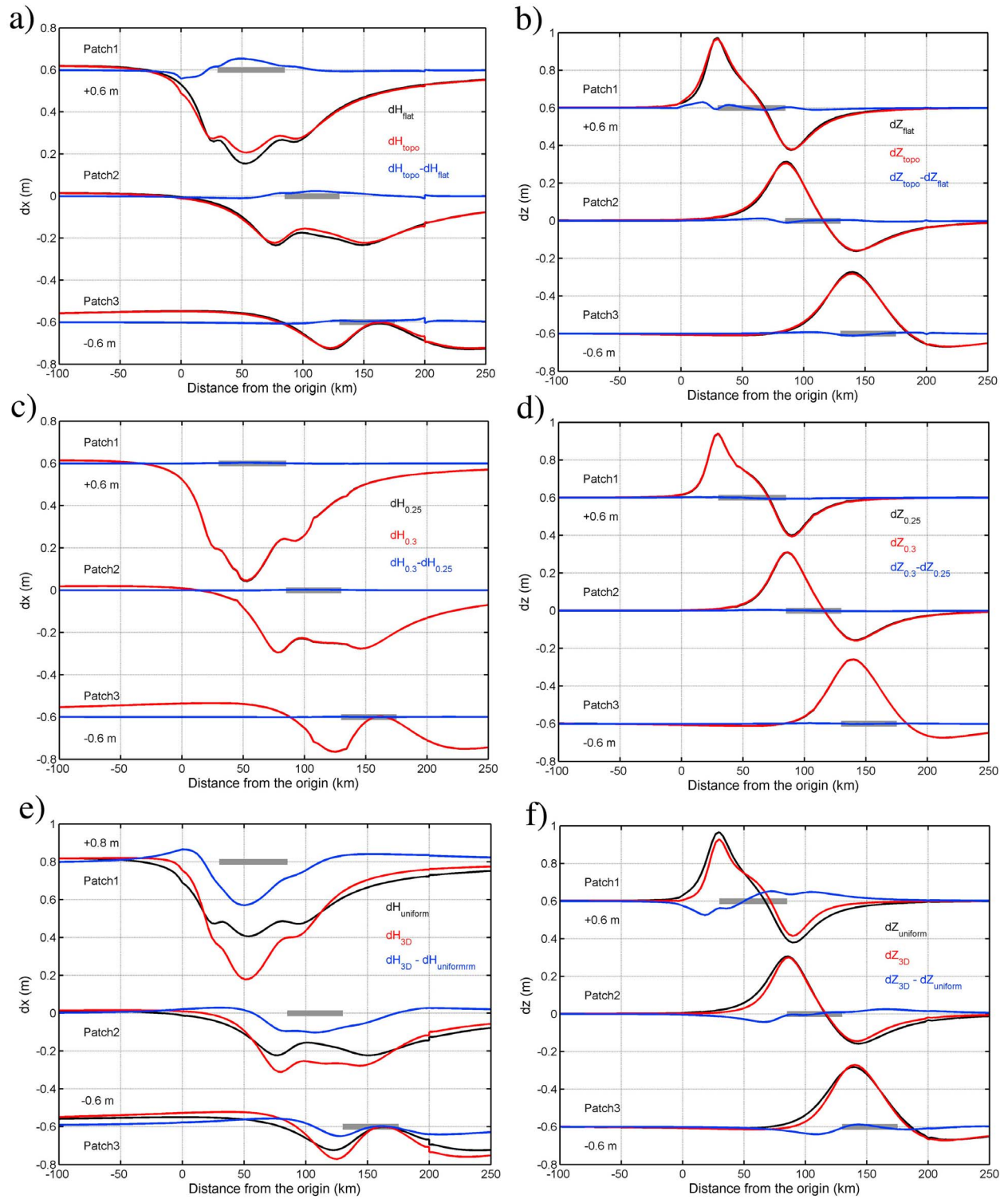


Figure 5



displacements are less affected by the complexity of the material heterogeneity at shallow depths. Note that if the source is steeply dipping, the vertical deformation would be more sensitive. These experiments suggest that the influences of topographic relief and material complexity on surface displacements depend on the position of rupture sources as well. To demonstrate this idea, we consider the constitutive equation for a linear elastic material in terms of Young's modulus (E) and Poisson's ratio (ν), which may be written as

$$\sigma_{ij} = \frac{E\nu\delta_{ij}\varepsilon_{kk}}{(1+\nu)(1-2\nu)} + \frac{E\varepsilon_{ij}}{(1+\nu)} \quad (1)$$

For plane strain conditions this yields

$$\begin{aligned} \sigma_{xx} &= \frac{\nu E(\varepsilon_{xx} + \varepsilon_{yy})}{(1+\nu)(1-2\nu)} + \frac{E\varepsilon_{xx}}{1+\nu} \\ \sigma_{yy} &= \frac{\nu E(\varepsilon_{xx} + \varepsilon_{yy})}{(1+\nu)(1-2\nu)} + \frac{E\varepsilon_{yy}}{1+\nu} \\ \sigma_{xy} &= \frac{E\varepsilon_{xy}}{1+\nu} \end{aligned} \quad (2)$$

In the case of homogeneous material properties, the equilibrium equations in the absence of body forces are

$$\begin{aligned} \frac{\partial\sigma_{xx}}{\partial x} + \frac{\partial\sigma_{xy}}{\partial y} &= 0 = \left[\frac{\nu E}{(1+\nu)(1-2\nu)} + \frac{E}{1+\nu} \right] \frac{\partial\varepsilon_{xx}}{\partial x} \\ &+ \frac{\nu E}{(1+\nu)(1-2\nu)} \frac{\partial\varepsilon_{yy}}{\partial x} + \frac{E}{1+\nu} \frac{\partial\varepsilon_{xy}}{\partial y} \\ \frac{\partial\sigma_{yy}}{\partial y} + \frac{\partial\sigma_{xy}}{\partial x} &= 0 = \left[\frac{\nu E}{(1+\nu)(1-2\nu)} + \frac{E}{1+\nu} \right] \frac{\partial\varepsilon_{yy}}{\partial y} \\ &+ \frac{\nu E}{(1+\nu)(1-2\nu)} \frac{\partial\varepsilon_{xx}}{\partial y} + \frac{E}{1+\nu} \frac{\partial\varepsilon_{xy}}{\partial x} \end{aligned} \quad (3)$$

If we consider the case where Young's modulus is no longer constant, but varies spatially $E = E(x, y)$, these equations can be written as

$$\begin{aligned} \left[\frac{\nu E}{(1+\nu)(1-2\nu)} + \frac{E}{1+\nu} \right] \frac{\partial\varepsilon_{xx}}{\partial x} + \frac{\nu E}{(1+\nu)(1-2\nu)} \frac{\partial\varepsilon_{yy}}{\partial x} \\ + \frac{E}{1+\nu} \frac{\partial\varepsilon_{xy}}{\partial y} &= - \left[\frac{\nu(\varepsilon_{xx} + \varepsilon_{yy})}{(1+\nu)(1-2\nu)} + \frac{\varepsilon_{xx}}{1+\nu} \right] \frac{\partial E}{\partial x} \\ - \frac{\varepsilon_{xy}}{1+\nu} \frac{\partial E}{\partial y} \\ \left[\frac{\nu E}{(1+\nu)(1-2\nu)} + \frac{E}{1+\nu} \right] \frac{\partial\varepsilon_{yy}}{\partial y} + \frac{\nu E}{(1+\nu)(1-2\nu)} \frac{\partial\varepsilon_{xx}}{\partial y} \\ + \frac{E}{1+\nu} \frac{\partial\varepsilon_{xy}}{\partial x} &= - \left[\frac{\nu(\varepsilon_{xx} + \varepsilon_{yy})}{(1+\nu)(1-2\nu)} + \frac{\varepsilon_{yy}}{1+\nu} \right] \frac{\partial E}{\partial y} \\ - \frac{\varepsilon_{xy}}{1+\nu} \frac{\partial E}{\partial x} \end{aligned} \quad (4)$$

In the case where Poisson's ratio is no longer constant, but varies spatially $\nu = \nu(x, y)$, these equations can be written as

$$\begin{aligned} \left[\frac{\nu E}{(1+\nu)(1-2\nu)} + \frac{E}{1+\nu} \right] \frac{\partial\varepsilon_{xx}}{\partial x} + \frac{\nu E}{(1+\nu)(1-2\nu)} \frac{\partial\varepsilon_{yy}}{\partial x} \\ + \frac{E}{1+\nu} \frac{\partial\varepsilon_{xy}}{\partial y} &= - \left[\frac{E(\varepsilon_{xx} + \varepsilon_{yy})(1+2\nu^2)}{(1+\nu)^2(1-2\nu)^2} - \frac{E\varepsilon_{xx}}{(1+\nu)^2} \right] \frac{\partial\nu}{\partial x} \\ + \frac{E\varepsilon_{xy}}{(1+\nu)^2} \frac{\partial\nu}{\partial y} \\ \left[\frac{\nu E}{(1+\nu)(1-2\nu)} + \frac{E}{1+\nu} \right] \frac{\partial\varepsilon_{yy}}{\partial y} + \frac{\nu E}{(1+\nu)(1-2\nu)} \frac{\partial\varepsilon_{xx}}{\partial y} \\ + \frac{E}{1+\nu} \frac{\partial\varepsilon_{xy}}{\partial x} &= - \left[\frac{E(\varepsilon_{xx} + \varepsilon_{yy})(1+2\nu^2)}{(1+\nu)^2(1-2\nu)^2} - \frac{E\varepsilon_{yy}}{(1+\nu)^2} \right] \frac{\partial\nu}{\partial y} \\ + \frac{E\varepsilon_{xy}}{(1+\nu)^2} \frac{\partial\nu}{\partial x} \end{aligned} \quad (5)$$

Comparing the expressions where E and ν are constant (equation (3)) with those where they are spatially variable (equations (4) and (5)), we see that terms associated with spatial variations of material properties on the right hand sides of equations (4) and (5) will act as if they were distributed sources. Thus, equations (4) and (5) show that inversions for earthquake slip parameters may be significantly biased when the material gradients and strain are large and the material gradients are not sufficiently well represented in the model.

[11] Alternatively, we can examine the deformation in terms of shear modulus (G) and bulk modulus (K), which are often used to describe the material resistance to shearing strain (e.g., faulting) and to a change in volume (e.g., volcano deformation), respectively. The shear modulus G can be written as

$$G = \frac{E}{2(1+\nu)} \quad (6)$$

According to the quotient rule in calculus

$$\begin{aligned} \frac{\partial G}{\partial E} &= \frac{1}{2(1+\nu)} - \frac{E}{2(1+\nu)^2} \frac{\partial\nu}{\partial E} \\ \frac{\partial G}{G} &= \frac{2(1+\nu)}{E} \left[\frac{\partial E}{2(1+\nu)} - \frac{E}{2(1+\nu)^2} \frac{\partial\nu}{\partial E} \right] \\ \frac{\partial G}{G} &= \frac{\partial E}{E} - \frac{\nu}{(1+\nu)} \frac{\partial\nu}{\nu} \end{aligned} \quad (7)$$

Assuming $\nu = 0.25$, $\frac{\partial G}{G} = \frac{\partial E}{E} - 0.2\left(\frac{\partial\nu}{\nu}\right)$, the same amount of perturbation in E can give rise to five times larger perturbation in G compared to that in ν . Since most earth materials have a value of ν between 0.22 and 0.35, the same amount of perturbation in E has a larger contribution to G compared to that in ν .



Table 2. Studied Parameters, Model Setup, Modeling Results, and Illustrations in This Study^a

Studied Parameter	Input	Output	Section and Figure
Topography	Coseismic slip distribution [Hsu et al., 2006]; fault geometry (fault <i>B</i> , Figure 3); 3-D elastic model (model <i>A</i> , Figure 4b)	Surface displacement	Section 4.1; Figures 6b and 6e
Poisson's ratio (ν)	Coseismic slip distribution [Hsu et al., 2006]; fault geometry (fault <i>B</i> , Figure 3); 3-D elastic model ($\nu = 0.25$ or 0.3 , model <i>A</i> , Figure 4a)	Surface displacement	Section 4.1; Figures 6c and 6f
Young's modulus (E)	Coseismic slip distribution [Hsu et al., 2006]; fault geometry (fault <i>B</i> , Figure 3); 3-D elastic model (Figure 4b)	Surface displacement	Section 4.2; Figure 7
Fault geometry; fault slip distribution (half - space model)	Coseismic slip distribution [Hsu et al., 2006]; surface coseismic displacements estimated by a 3-D elastic model (model <i>B</i> , Figure 4b)	Surface displacement; fault geometry; fault slip distribution; vertical residuals	Section 4.3; Figure 8
Fault geometry; fault slip distribution (layered earth model)	Coseismic slip distribution [Hsu et al., 2006]; surface coseismic displacements estimated by a 3-D elastic model (model <i>B</i> , Figure 4b)	Surface displacement; fault geometry; fault slip distribution; vertical residuals	Section 4.3; Figure 9
Fault slip distribution; (fixed w_{rms} value)	Coseismic slip distribution [Hsu et al., 2006]; fault geometry (fault <i>B</i> , Figure 3); 3-D elastic models (models <i>HS</i> and <i>A-C</i> , Figure 4b)	Surface displacement; fault slip distribution; vertical residuals	Section 4.4; Figure 10; Table 3
Fault geometry; fault slip; coseismic potency	Coseismic observations [Hsu et al., 2006]; fault geometry (fault <i>A-C</i> , Figure 3); 3-D elastic models (models <i>HS</i> and <i>A-C</i> , Figure 4b)	Coseismic potency; maximum slip; average slip; w_{rms}	Section 4.5; Table 3

^aAbbreviation: w_{rms} , weighted root-mean-square misfit.

[12] On the other hand, the bulk modulus K can be written as

$$K = \frac{E}{3(1 - 2\nu)} \quad (8)$$

According to the quotient rule

$$\begin{aligned} \frac{\partial K}{\partial E} &= \frac{1}{3(1 - 2\nu)} + \frac{2E}{3(1 + \nu)^2} \frac{\partial \nu}{\partial E} \\ \frac{\partial K}{K} &= \frac{3(1 - 2\nu)}{E} \left[\frac{\partial E}{3(1 - 2\nu)} + \frac{2E}{3(1 - 2\nu)^2} \partial \nu \right] \\ \frac{\partial K}{K} &= \frac{\partial E}{E} + \frac{2\nu}{(1 - 2\nu)} \frac{\partial \nu}{\nu} \end{aligned} \quad (9)$$

Assuming $\nu = 0.25$, $\frac{\partial K}{K} = \frac{\partial E}{E} + \left(\frac{\partial \nu}{\nu}\right)$, the perturbations in ν and E have the same contribution in K . If $\nu = 0.35$, the same amount of perturbation in ν can cause 2.3 times larger perturbation in K compared to that in E . These equations show that the variation of Poisson's ratio may play an important role when ν is larger than 0.25 and the rupture source is dilatational such as volcano deformation.

4. Results and Discussion: 3-D FEM Models of the 2005 Nias-Simeulue Earthquake

[13] In this section, we discuss different parameters in the finite element modeling of the 2005 earth-

quake and summarize all tests, their respective goals, and numbers of related figures in Table 2.

4.1. Impact of Topography and Poisson's Ratio on Surface Displacements

[14] Inversions on fault slip distributions using elastic half-space or layered earth models often assume that the top surface is flat. However, topographic relief near the Sunda subduction zone can be as large as 6 km (Figure 3). To examine the effect of topographic relief on coseismic surface deformation of the 2005 earthquake, we compare surface coseismic displacements from a model with a flat surface to one with more realistic topographic relief, both using the same input slip model [Hsu et al., 2006]. The predicted horizontal surface displacements from the model with realistic topography are generally larger than those in a flat earth model (Figure 6b). Predicted vertical displacements from the two models show systematic differences in predicted surface displacements as a function of distance from the Sunda trench (Figure 6e). The model with realistic topography shows that the actual depth of the top surface is deeper on the western side of the Sunda trench and shallower on the eastern side compared to a flat earth model (Figures 6d and 6e). Therefore, predicted vertical displacements are underestimated and overestimated to the west and east sides, respectively, of the trench in the flat earth model. We do not observe

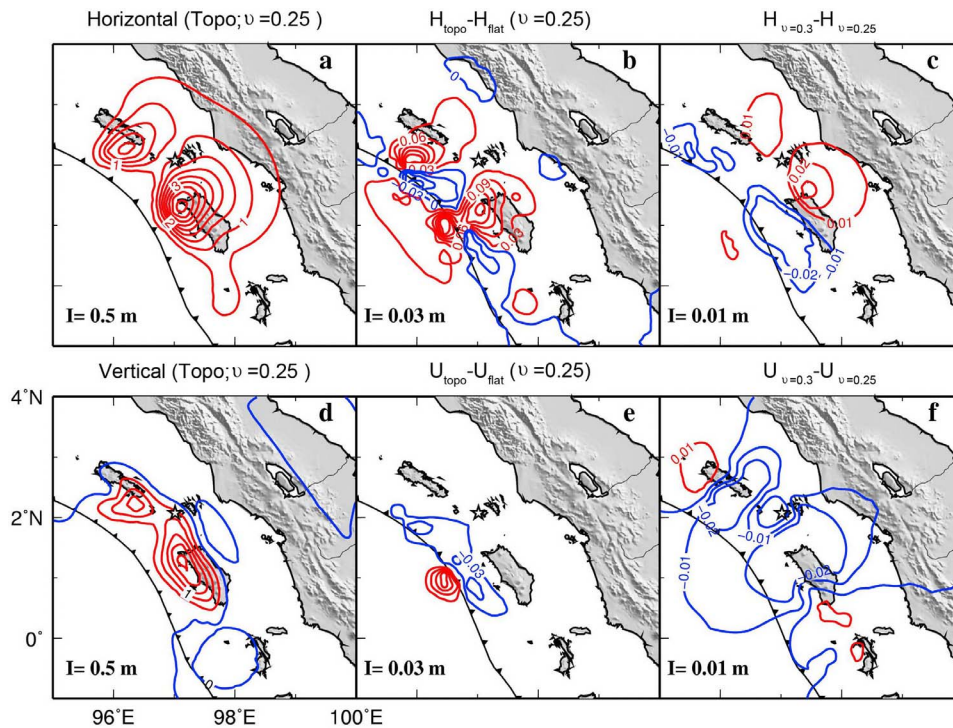


Figure 6. Contour of coseismic surface displacements and differences between various models. The contour interval for each panel is shown as black text at the bottom left corner. The black barbed line indicates the Sunda megathrust. The star denotes the epicenter of 2005 earthquake. (a) Surface horizontal displacements estimated from coseismic slip on fault *B* (Figure 3). (b) Differences in horizontal displacements between models with a flat top surface and with topographic relief. Red and blue colors indicate positive and negative differences. (c) Differences in horizontal displacements between models with Poisson's ratio of 0.25 and 0.3, respectively. (d) Vertical displacements estimated from coseismic slip on fault *B* (Figure 3). (e and f) Similar to Figure 6b and 6c but for differences in vertical displacements.

significant systematic difference in horizontal displacements between these two models, which is possibly due to 3-D variations of coseismic slip along the trench resulting in a more complex horizontal displacement field compared to the vertical displacement. In summary, the maximum difference between two models is about 5% and mainly localized near the trench where the topographic gradient is highest (Figures 6b and 6e). While not large, these differences are sufficiently systematic that for all subsequent models, we use realistic estimates of topographic relief.

[15] Studies from petrographic and geochemical analyses [Bebout and Barton, 1993], laboratory experiments [Peacock, 1990; Moore and Vrolijk, 1992; Moore and Saffer, 2001], and inferences from magnetotelluric measurements [Wei et al., 2001] and seismic tomography [Zhao et al., 2000] suggest the existence of fluid in subduction thrust faults. The Poisson's ratio increases with fluid content and pressure and also varies according to the fluid content conditions and rock composition

[Christensen, 1996; Turcotte and Schubert, 2002], thus the assumption of a Poisson solid (Poisson's ratio of 0.25) in the elastic dislocation mode is not necessarily appropriate. To examine the effect of Poisson's ratio on surface deformation, we calculate surface coseismic displacements with Poisson's ratio of 0.25 and 0.3, respectively. These two models differ by only 2% (Figures 6c and 6f). Owing to this apparent insensitivity to perturbations of Poisson's ratio, henceforth we fix Poisson's ratio to the value of 0.25.

4.2. Surface Displacements Computed From Heterogeneous Elastic Models

[16] To test the effect of 3-D elastic heterogeneity, we partition our model into six regions with values of density and Young's modulus (Table 1 and Figure 4a) chosen in accordance with data from seismic refractions in the Sunda trench and nearby fore-arc basins [Kieckhefer et al., 1980, 1981]. Here, we use the ratio of Young's modulus to the minimum value in the heterogeneous elastic model

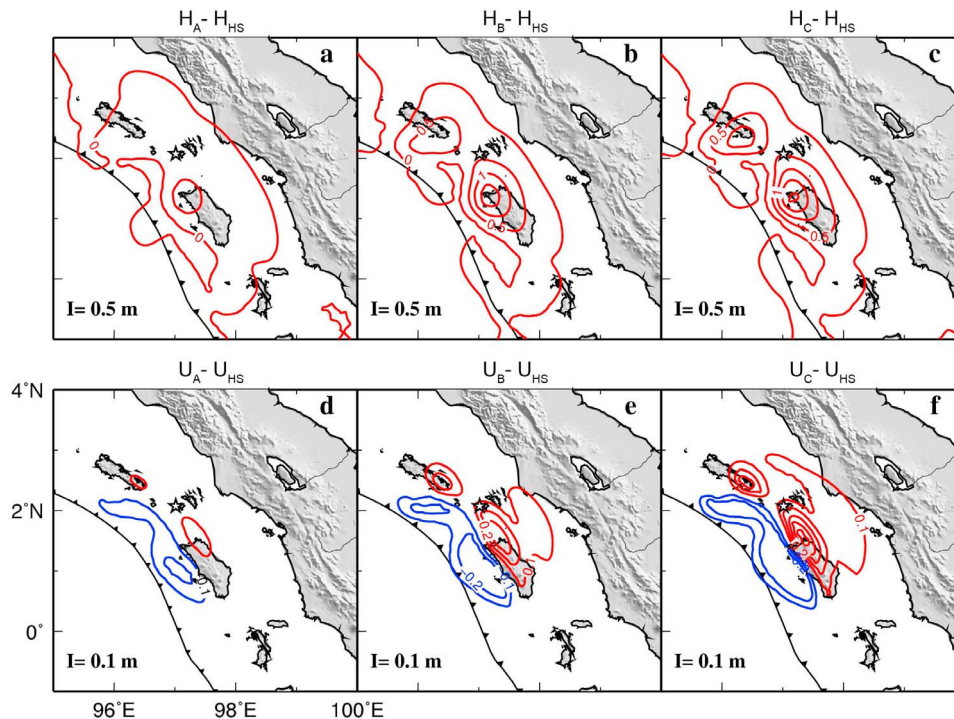


Figure 7. Differences in coseismic surface displacements between homogeneous and heterogeneous material models (Figure 4b) based on the same slip model. The contour interval for each panel is shown as black text on the bottom left corner. Red and blue colors indicate that surface displacements in heterogeneous models are larger and smaller than those in model *HS*. The star denotes the epicenter of 2005 earthquake. (a–c) Differences in horizontal displacements between model *HS* and model *A*, model *HS* and model *B*, and model *HS* and model *C*. (d–f) Similar to Figures 7a–7c but for differences in vertical displacements.

(E/E_{\min}). The material model *B* is our preferred model (Figure 4b). We test three different heterogeneous models with increasing contrast between the upper accretionary wedge and the rest of the structural blocks (Figure 4b).

[17] To begin with, we use the same coseismic slip model [Hsu *et al.*, 2006] and the fault geometry (fault *B* in Figure 3) to estimate surface displacements. The directions of surface horizontal displacements in all heterogeneous elastic models (models *A–C* in Figure 4b) are not much different from those in the homogeneous model (model *HS* in Figure 4b). However, magnitudes in models *A–C* are amplified due to soft unconsolidated sediments in accretionary wedge. The vertical surface displacements are less affected by soft layer at shallow depths. The differences in maximum surface displacements between model *HS* and model *A*, model *HS* and model *B*, and model *HS* and model *C* are about 15%, 35%, and 40%, respectively (Figure 7). Note that differences of surface displacements between homogeneous and heterogeneous models vary significantly depending on material properties.

4.3. Inverted Coseismic Slip and Fault Geometry in a Simplified Earth Model Using Synthetic Displacements From a Heterogeneous Elastic Model

[18] Elastic half-space and layered earth models are commonly used in studies of crustal deformation. The preceding tests beg the question of how well a half-space model and a layered earth model can fit surface displacements estimated from a complex 3-D elastic structure. We estimate the synthetic surface displacements on CGPS and coral sites using fault *B* (Figure 3), material model *B* (Figure 4b), realistic topography, and estimated coseismic slip distribution from Hsu *et al.* [2006]. The errors in synthetic surface displacements are assigned to be the observational errors of coseismic displacements. However, we reduce the amplitude of observational errors by a factor of 4 in coral sites to obtain a better fit in vertical displacements. After adjustments, the average standard deviation in CGPS and coral sites are 4.3 and 6 mm, respectively.

[19] We then use elastic half-space and layered earth models to invert for the optimal slip distribu-

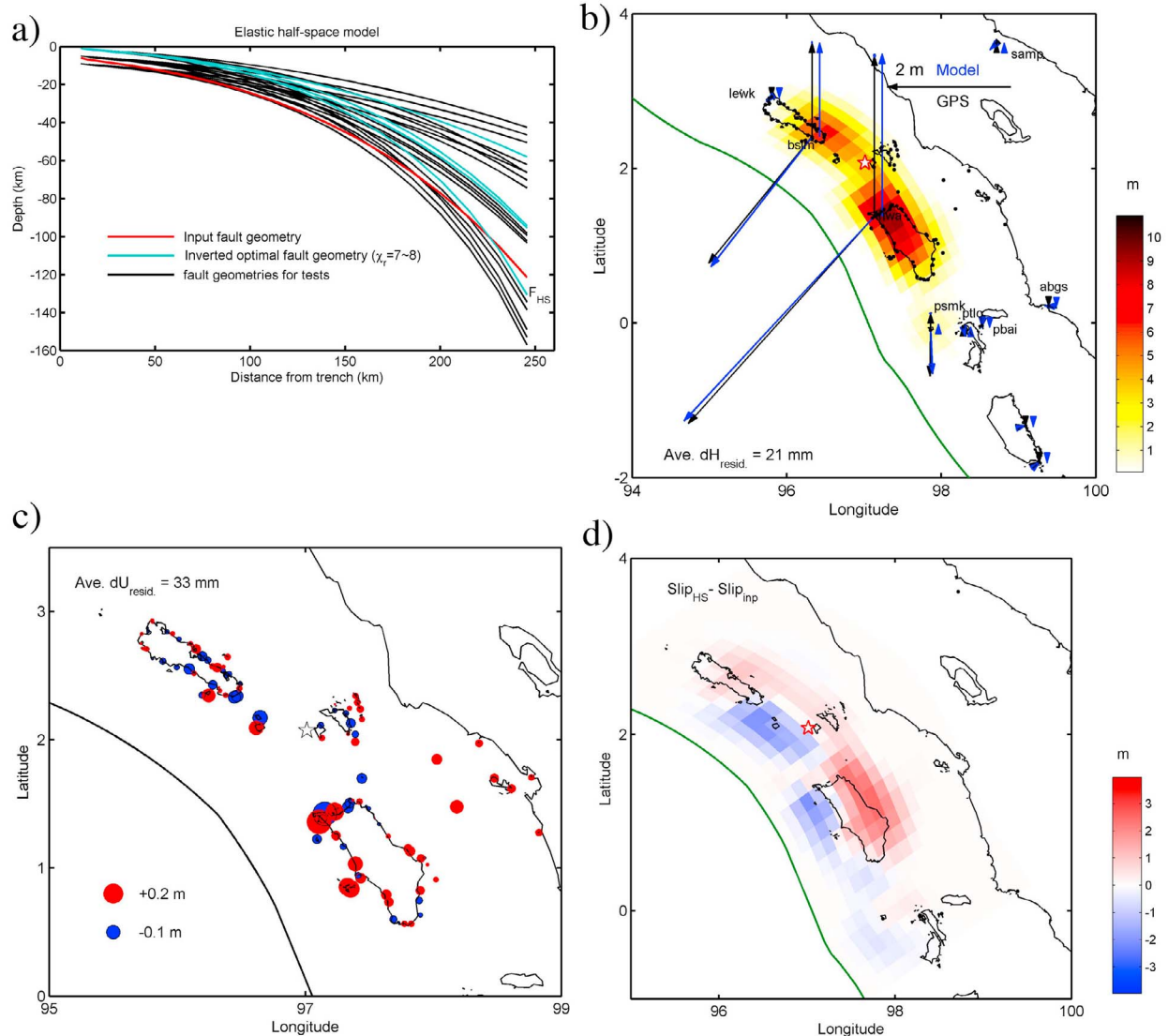


Figure 8. Inverted coseismic slip and fault geometry in a half-space earth model using synthetic displacements from a heterogeneous elastic model (a) The input fault model (red curve) and a variety of testing fault models (black curve). The optimal models with values of reduced chi-square of 7–8 are shown in blue curves. (b) Slip distribution on the fault, F_{HS} , in Figure 8a is shown in color. The black and blue vectors show the observed and predicted horizontal GPS displacements. (c) Residuals of the vertical displacements. Red and blue circles indicate predicted values are larger and smaller than observations, respectively. (d) The difference in coseismic slip between Figure 8b and the input slip model.

tion and the fault geometry that can best fit synthetic displacements. The layered elastic model used here is a simplified version of model *B* (Figure 4b), which is composed of three layers. The reduced chi-square value (χ_r^2) is used to evaluate the model fit. A value of 1 means that the model fits the data within uncertainties. By searching a wide range of fault geometries, we cannot find a satisfactory fit to the synthetic displacements using simplified earth models. The values of reduced chi-square in all testing fault modes are larger than 7 in an elastic

half-space model and larger than 9 in a layered earth model. We define the optimal fault geometries as those resulting in reduced chi-square values ranging from 7 to 8 in an elastic half-space model (Figure 8) and 9 to 10 in a layered earth model (Figure 9). The modeling results show various fault geometries with similar fits to synthetic surface displacements. Comparing the real fault geometry (the red curves in Figures 8a and 9a) to a family of optimal fault geometries (the blue curves in Figures 8a and 9a), the results from both elastic half-space and layered

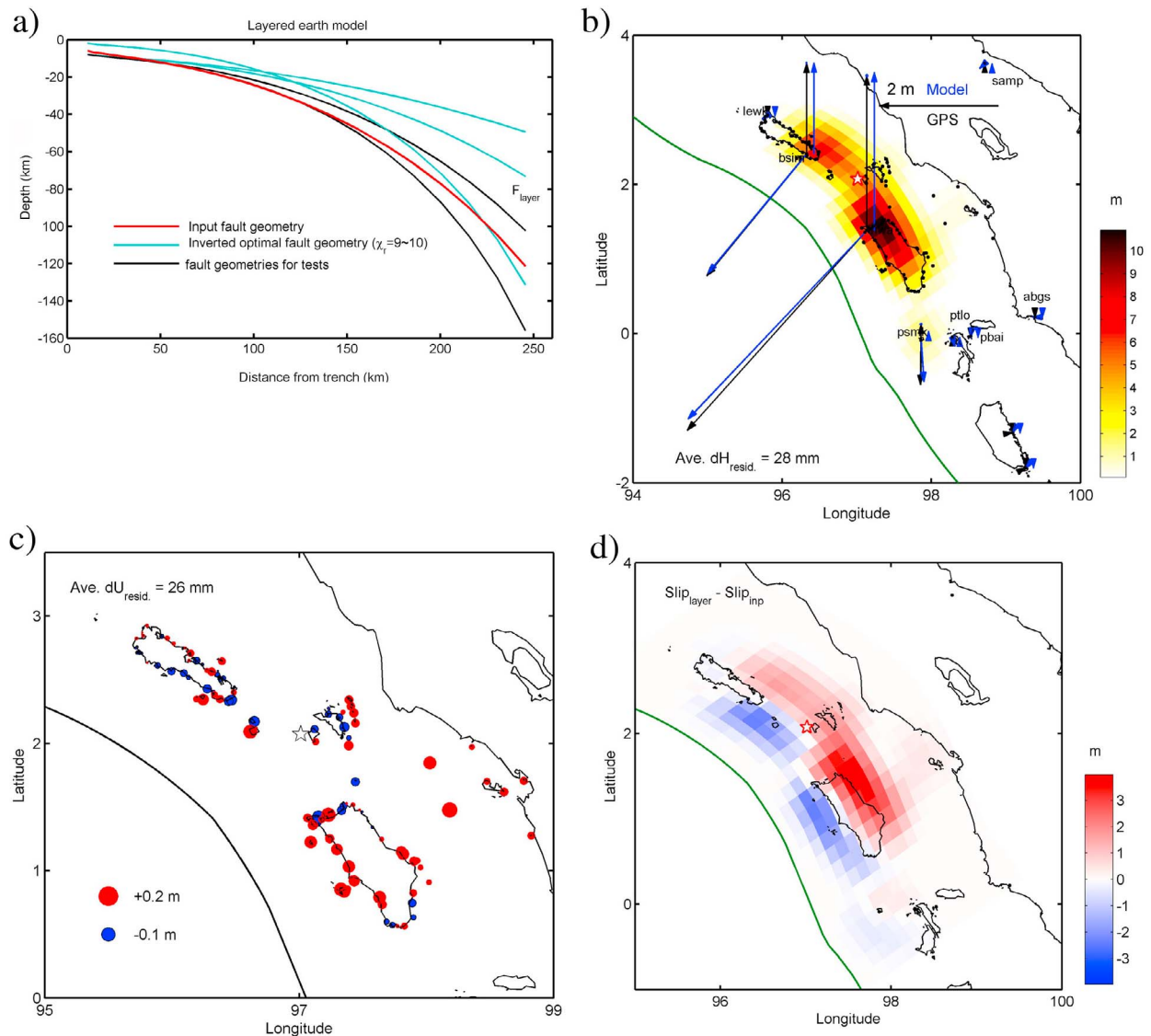


Figure 9. Inverted coseismic slip and fault geometry in a layered earth model using synthetic displacements from a heterogeneous elastic model. (a) The input fault model (red curve) and a variety of testing fault models (black curve). The optimal models with values of reduced chi-square of 9–10 are shown in blue curves. (b) Slip distribution on the fault, F_{layer} , in Figure 9a is shown in color. The black and blue vectors show the observed and predicted horizontal GPS displacements. (c) Residuals of the vertical displacements. Red and blue circles indicate predicted values are larger and smaller than observations, respectively. (d) The difference in coseismic slip between Figure 9b and the input slip model.

models tend to underestimate the actual depth of the real fault.

[20] We choose one fault model, F_{HS} (blue curve indicated in Figure 8a), which is closest to the input fault model, and compare the slip distribution and predicted surface displacements with the input slip and surface displacements (Figures 8b–8d). We find predicted horizontal displacements from the elastic half-space model can reasonably fit synthetic

displacements (Figure 8b). However, residuals in the vertical displacements show a systematic misfit (Figure 8c). On the other hand, predicted surface displacements using a fault model, F_{layer} (Figure 9a) and a layered earth structure also show similar features as those in Figure 8.

[21] We find that none of these inferred slip distributions are close to the input slip model. Models with simplified Green's functions apparently map



Table 3. Values of Weighted Root-Mean-Square Misfit, Maximum Coseismic Slip, Average Slip, and Coseismic Potency of All Models^a

	Fault A				Fault B				Fault C			
	HS	A	B	C	HS	A	B	C	HS	A	B	C
<i>Values of Weighted Root-Mean-Square Misfit Fixed to 0.0649 m</i>												
S_{\max} (m)	10.2	12.3	12.8	13.5	11.2	10.6	10.1	10.1	12.7	11.5	10.5	10.0
S_{mean} (m)	1.1	0.9	0.8	0.8	1.2	0.9	0.8	0.8	1.2	1.1	1.0	0.9
Potency ($\text{km}^2 \times \text{m}$)	164,860	152,700	134,000	125,890	176,150	159,560	138,470	131,910	185,910	179,460	163,060	156,120
<i>Optimal Model Determined by Cross Validation</i>												
w_{rms} (m)	0.0552	0.0691	0.0810	0.0895	0.0612	0.0649	0.0665	0.0678	0.0697	0.0668	0.0648	0.0629
S_{\max} (m)	10.7	12.0	11.7	11.7	11.5	10.6	9.9	9.9	12.0	11.2	10.5	10.2
S_{mean} (m)	1.0	0.9	0.9	0.9	1.1	0.9	0.8	0.8	1.3	1.1	1.0	0.9
Potency ($\text{km}^2 \times \text{m}$)	148,790	156,720	144,370	140,850	168,410	159,560	140,990	136,030	198,180	184,220	162,800	151,860

^aMaterial models: *HS*, *A*, *B*, and *C*. Abbreviations: S_{\max} , maximum coseismic slip; S_{mean} , average coseismic slip; potency, product of slip and slip area; w_{rms} , weighted root-mean-square misfit.

errors in 3-D elastic structures back into fault slip. The slip distributions derived from simplified earth models underestimate the coseismic potency and the centroid depth of the actual fault, consistent with the findings on coseismic slip models of strike-slip fault with increasing E at depths [Rybicki and Kasahara, 1977; Savage, 1987; Hearn and Burgmann, 2005].

4.4. Coseismic Slip Distributions Using FEM Derived Elastic Green's Functions

[22] As found previously [Masterlark *et al.*, 2001; Masterlark, 2003] and as just demonstrated, surface displacements are significantly influenced by 3-D variations of material properties. To evaluate the effect of heterogeneous material properties on the inferred spatial distribution of coseismic slip, we use the fault geometry *B* in Figure 3 and realistic topography to compute 3-D Green's functions at fault slip node pairs. The displacements on the surface nodes resulting from a unit dislocation of a fault split node pair are used to interpolate displacements at all CGPS and coral sites. We then create Green's functions composed of displacement components at each site. In this experiment, there are five versions of Green's functions including a homogeneous model (model *HS*, Figure 4), a layered earth model from earth structure CRUST2.0 [Bassin *et al.*, 2000], as well as three heterogeneous elastic models (models *A*, *B*, *C*; Figure 4b). We invert for coseismic slip using the same inversion scheme as Hsu *et al.* [2006], a weighted least squares algorithm with two forms of regularization: Laplacian smoothing and moment minimization. Because characteristics of the inferred models differ as a function of model roughness, data misfits and model solution length, we compare models

with the same weighted root-mean-square misfit (w_{rms} , listed in Table 3).

[23] The differences in inferred coseismic slip for the layered model and the other heterogeneous models (Figure 4b) relative to model *HS* are shown in Figure 10. In general, the fits of horizontal displacements improve if the contrast between the upper accretionary wedge and the rest of the structural model is increased. In all models, we find systematic misfits in vertical displacements corresponding to the features observed in our synthetic tests (Figures 8c and 9c). These systematic misfits might imply that the elastic contrast in geological material models used in this study needs to be adjusted to obtain a better fit to the vertical displacements or more complex fault geometry is required. An alternative source of systematic vertical misfit is possibly associated with large observational errors in coral measurements compared to those in horizontal GPS displacements.

[24] The maximum coseismic slip decreases with increases in rigidity contrast between the upper wedge and surrounding material blocks (Table 3 and Figure 10). For instance, the maximum coseismic slip of 10.1 m in model *C* is 10% less than 11.2 m in model *HS*. Figure 10 shows differences of coseismic slip in various elastic models relative to that in a homogeneous model (model *HS*). Discrepancies in fault slip between model *HS* and other material models get bigger when the elastic contrast between the two sides of the fault is increased. Compared to model *HS*, the coseismic slip derived from a layered earth structure, CRUST2.0 [Bassin *et al.*, 2000], is less as illustrated in Figure 10a. The weak geological material on the top layer is likely to amplify surface displacements hence the layered

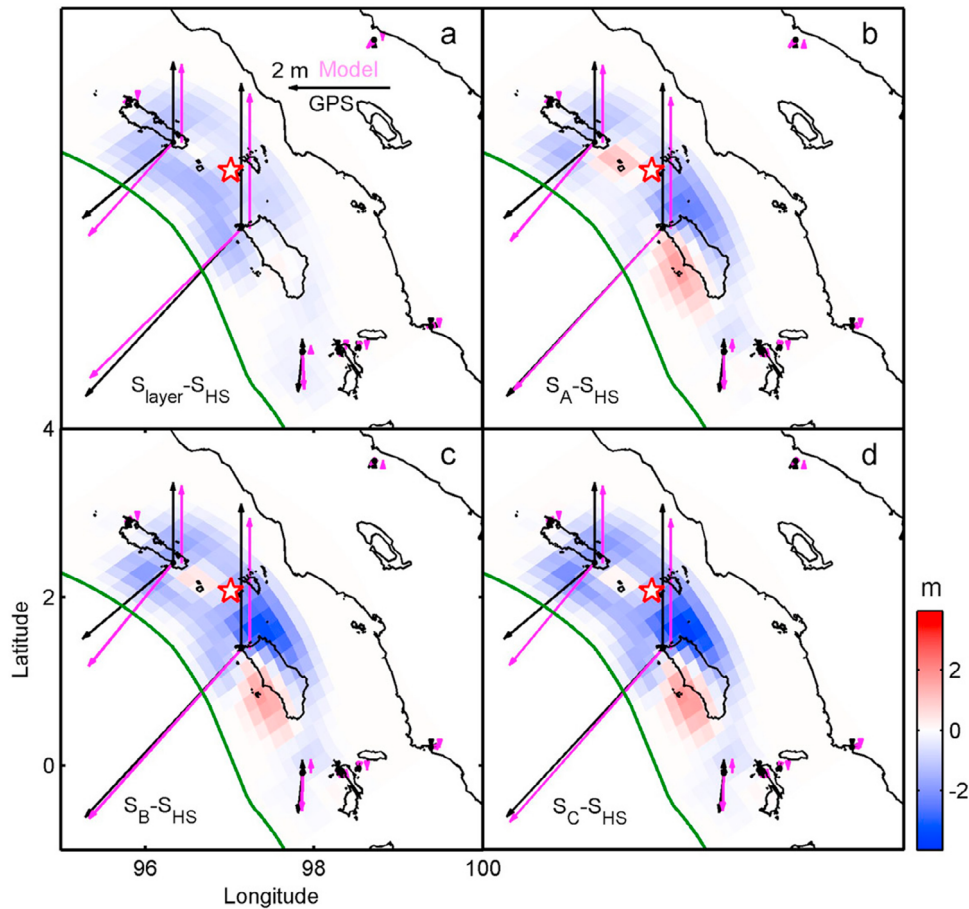


Figure 10. Differences between inferred coseismic slip models and model *HS* (color scale) and fits to GPS observations using (a) a layered model and (b–d) three heterogeneous elastic models (models *A–C* in Figure 4b). Black and pink vectors indicated observed and predicted GPS displacements. The star indicates the epicenter. Green curved line denotes the location of trench.

and heterogeneous elastic models require a small amount of slip on the fault (Figure 10 and Table 3).

[25] Coseismic slip close to the trench is generally small in heterogeneous material models, in contrast to significant updip slip from the coseismic rupture in model *HS* (Figure 10). We find heterogeneous models (models *A*, *B*, *C*) require less updip slip and downdip slip compared to the homogeneous model (model *HS*). Total coseismic potency in model *C* decreases by 20% compared to that in model *HS* (Table 3). This feature suggests that estimates on geodetic moment or stress variations at depth may be biased by the assumption of a uniform earth.

4.5. Coseismic Slip Distributions Derived From Various Fault Geometries

[26] Finally, we compare optimal coseismic slip distributions inverted from different combinations

of fault geometries (Figure 3) and heterogeneous elastic models (Figure 4b). All these models incorporate regional topographic variations. We choose damping parameters using cross validation and do not constrain values of *wrms* to be the same.

[27] We use three different candidate fault geometries (faults *A–C* in Figure 3) to address the relationship between coseismic slip and 3-D elastic heterogeneity. Integrated coseismic potency decreases with the increasing rigidity contrast between the upper accretionary wedge and surrounding materials independent of fault geometry (Table 3). The rupture area is narrower in heterogeneous material models, models *A–C*, than in model *HS*, which is also a common feature regardless of fault geometry. However, the maximum coseismic slip does not always decrease with increasing rigidity contrast across the fault. For example, inferred maximum coseismic slip on fault *A* in model *C* is larger



than that in model *HS*, which is opposite to the results using fault geometries of fault *B* or fault *C* (Table 3). The peak slip at depth differs between the various assumed fault geometries. Not surprisingly, a shallow fault requires less coseismic slip to fit surface displacements compared to a deep fault.

[28] To find the optimal coseismic model from a combination of various fault geometry and 3-D elasticity, we choose the damping parameter according to cross validation. Details of optimal coseismic models, fault geometries, and material properties are listed in Table 3. We note that values of *wrms* in 3-D elastic structure models are similar to those in the homogeneous model except for fault *A*. The fit to surface observations in the 3-D FEM model is similar to that in a simple half-space model. This similarity possibly results from the fact that the faults considered in our study are constructed according to the fault model determined from joint inversions of geodetic and seismic data with the assumption of a layered elastic earth model [Hsu et al., 2006]. We find that none of the fault models listed in Table 3 can fit the observed data within uncertainties. Due to limitations in our knowledge of real fault geometry and 3-D elastic structure, it is not reasonable to evaluate modeling results only by the fit to the data. The coseismic model using the fault geometry *B* (Figure 3) and the material model *B* (Figure 4b), is constrained by data from seismicity and seismic refractions. Although the fit to surface observations is similar to the result from a simple half-space model, the resulting slip distribution may reflect the true fault slip behavior with more fidelity. Given these results, we believe that the best strategy is to constrain fault geometries and 3-D elastic structures based on a priori information. Then we can perturb fault geometries or material properties using inversions. However, this procedure is computationally challenging when we require a new finite element mesh for each fault geometry.

5. Conclusion

[29] We explored the impact of adopting a realistic earth model on predictions of surface deformation using 3-D finite element modeling techniques. Surface displacements are more sensitive to variations in Young's modulus than to variations in topography and Poisson's ratio. The influence of 3-D variations in elastic properties and topography on surface displacements is significant if the fault slip (or more precisely, gradients in fault slip) occur close to gradients in rigidity or topography, with

the free surface being an extreme example of this case.

[30] If we generate synthetic displacements using a heterogeneous elastic model and then use an elastic half-space or layered earth model to estimate the slip distribution, we are unable to find any coseismic slip distribution that fits the synthetic surface GPS observations within the uncertainties. The coseismic potency and the centroid depth of the fault are underestimated, with systematic residuals in vertical displacements for the simplified earth models. The coseismic potencies resulted from slip models with the same misfits are less in all tested heterogeneous elastic models compared to that in a half-space model based on the same fault geometry.

[31] Using our preferred 3-D heterogeneous elastic model to study the coseismic deformation of the 2005 Sumatra earthquake, we find that the fit to the surface displacements is similar to that of an elastic half-space model. However, our model takes into account available observations of elastic properties near the rupture area and may reflect a more realistic distribution of fault slip. We find that direct inversion of the fault geometry and slip distribution from GPS and coral data is generally a poorly constrained problem. Moreover, the remaining misfit implies that the true elastic structure and/or fault geometry might be more complex than our preferred model or that there are other deformation mechanisms taking place during earthquake ruptures, such as slip on splay faults or inelastic deformation.

Acknowledgments

[32] We thank the Editor, Thorsten Becker, and two reviewers, Tim Masterlark and an anonymous reviewer, for their thoughtful reviews and valuable comments that helped to improve the manuscript. This study was supported by the Institute of Earth Sciences, Academia Sinica, the National Science Council of the Republic of China grant NSC 98-2119-M-001-033-MY3. This is a contribution of the Institute of Earth Sciences, Academia Sinica, IESAS1590, Caltech Seismological Laboratory contribution number 10061, and Caltech Tectonics Observatory contribution number 175.

References

- Bassin, C., G. Laske, and G. Masters (2000), The current limits of resolution for surface wave tomography in North America, *Eos Trans. AGU*, 81(48), Fall Meet. Suppl., Abstract S12A-03.
- Bebout, G. E., and M. D. Barton (1993), Metasomatism during subduction: Products and possible paths in the Catalina schist, California, *Chem. Geol.*, 108, 61–92, doi:10.1016/0009-2541(93)90318-D.



- Briggs, R. W., et al. (2006), Deformation and slip along the Sunda megathrust in the great 2005 Nias-Simeulue earthquake, *Science*, *311*, 1897–1901.
- Chlieh, M., et al. (2007), Coseismic slip and afterslip of the great M_w 9.15 Sumatra-Andaman earthquake of 2004, *Bull. Seismol. Soc. Am.*, *97*, S152–S173, doi:10.1785/0120050631.
- Christensen, N. I. (1996), Poisson's ratio and crustal seismology, *J. Geophys. Res.*, *101*, 3139–3156, doi:10.1029/95JB03446.
- Du, Y. J., P. Segall, and H. J. Gao (1994), Dislocations in inhomogeneous-media via a moduli perturbation approach: General formulation and two-dimensional solutions, *J. Geophys. Res.*, *99*, 13,767–13,779, doi:10.1029/94JB00339.
- Engdahl, E. R., A. Villasenor, H. R. DeShon, and C. H. Thurber (2007), Teleseismic relocation and assessment of seismicity (1918–2005) in the region of the 2004 M_w 9.0 Sumatra-Andaman and 2005 M_w 8.6 Nias Island great earthquakes, *Bull. Seismol. Soc. Am.*, *97*, S43–S61, doi:10.1785/0120050614.
- Fialko, Y. (2006), Interseismic strain accumulation and the earthquake potential on the southern San Andreas fault system, *Nature*, *441*, 968–971, doi:10.1038/nature04797.
- Graves, R. W., and D. J. Wald (2001), Resolution analysis of finite fault source inversion using one- and three-dimensional Green's functions: 1. Strong motions, *J. Geophys. Res.*, *106*, 8745–8766, doi:10.1029/2000JB900436.
- Hearn, E. H., and R. Burgmann (2005), The effect of elastic layering on inversions of GPS data for coseismic slip and resulting stress changes: Strike-slip earthquakes, *Bull. Seismol. Soc. Am.*, *95*, 1637–1653, doi:10.1785/0120040158.
- Hsu, Y. J., M. Simons, S. B. Yu, L. C. Kuo, and H. Y. Chen (2003), A two-dimensional dislocation model for interseismic deformation of the Taiwan mountain belt, *Earth Planet. Sci. Lett.*, *211*, 287–294, doi:10.1016/S0012-821X(03)00203-6.
- Hsu, Y. J., M. Simons, J. P. Avouac, J. Galetzka, K. Sieh, M. Chlieh, D. Natawidjaja, L. Prawirodirdjo, and Y. Bock (2006), Frictional afterslip following the 2005 Nias-Simeulue earthquake, Sumatra, *Science*, *312*, 1921–1926, doi:10.1126/science.1126960.
- Huang, B. S., and Y. T. Yeh (1997), Effect of near-fault terrain upon dislocation modeling, *Pure Appl. Geophys.*, *150*, 1–18, doi:10.1007/s000240050060.
- Kieckhefer, R. M., G. G. Shor, J. R. Curray, W. Sugiarta, and F. Hehuwat (1980), Seismic refraction studies of the Sunda trench and fore-arc basin, *J. Geophys. Res.*, *85*, 863–889, doi:10.1029/JB085iB02p00863.
- Kieckhefer, R. M., G. F. Moore, and F. J. Emmel (1981), Crustal structure of the Sunda fore-arc region west of central Sumatra from Gravity data, *J. Geophys. Res.*, *86*, 7003–7012, doi:10.1029/JB086iB08p07003.
- Lohman, R. (2007), Generating Green's functions with PyLith, paper presented at Workshop on Community Finite Element Models for Fault Systems and Tectonic Studies, Golden, Colo., 25–29 June.
- Masterlark, T. (2003), Finite element model predictions of static deformation from dislocation sources in a subduction zone: Sensitivities to homogeneous, isotropic, Poisson solid, and half-space assumptions, *J. Geophys. Res.*, *108*(B11), 2540, doi:10.1029/2002JB002296.
- Masterlark, T., and K. L. H. Hughes (2008), Next generation of deformation models for the 2004 M9 Sumatra-Andaman earthquake, *Geophys. Res. Lett.*, *35*, L19310, doi:10.1029/2008GL035198.
- Masterlark, T., C. DeMets, H. F. Wang, O. Sanchez, and J. Stock (2001), Homogeneous vs heterogeneous subduction zone models: Coseismic and postseismic deformation, *Geophys. Res. Lett.*, *28*, 4047–4050, doi:10.1029/2001GL013612.
- McTigue, D. F., and P. Segall (1988), Displacements and tilts from dip-slip faults and magma chambers beneath irregular surface topography, *Geophys. Res. Lett.*, *15*, 601–604, doi:10.1029/GL015i006p00601.
- Melosh, H. J., and A. Raefsky (1981), A simple and efficient method for introducing faults into finite element computations, *Bull. Seismol. Soc. Am.*, *71*, 1391–1400.
- Moore, J. C., and D. Saffer (2001), Updip limit of the seismogenic zone beneath the accretionary prism of southwest Japan: An effect of diagenetic to low-grade metamorphic processes and increasing effective stress, *Geology*, *29*, 183–186, doi:10.1130/0091-7613(2001)029<0183:ULOTSZ>2.0.CO;2.
- Moore, J. C., and P. Vrolijk (1992), Fluids in accretionary prisms, *Rev. Geophys.*, *30*, 113–135, doi:10.1029/92RG00201.
- Okada, Y. (1985), Surface deformation due to shear and tensile faults in a half-space, *Bull. Seismol. Soc. Am.*, *75*, 1135–1154.
- Okada, Y. (1992), Internal deformation due to shear and tensile faults in a half-space, *Bull. Seismol. Soc. Am.*, *82*, 1018–1040.
- Peacock, S. M. (1990), Fluid processes in subduction zones, *Science*, *248*, 329–337, doi:10.1126/science.248.4953.329.
- Reilinger, R. E., et al. (2000), Coseismic and postseismic fault slip for the 17 August 1999, $M = 7.5$, Izmit, Turkey earthquake, *Science*, *289*, 1519–1524, doi:10.1126/science.289.5484.1519.
- Rundle, J. B. (1980), Static elastic-gravitation deformation of a layered half-space by point couple sources, *J. Geophys. Res.*, *85*, 5355–5363, doi:10.1029/JB085iB10p05355.
- Rybicki, K., and K. Kasahara (1977), Strike-slip fault in a laterally inhomogeneous-medium, *Tectonophysics*, *42*, 127–138, doi:10.1016/0040-1951(77)90164-0.
- Sandwell, D. T., and W. H. F. Smith (1997), Marine gravity anomaly from Geosat and ERS 1 satellite altimetry, *J. Geophys. Res.*, *102*, 10,039–10,054, doi:10.1029/96JB03223.
- Sato, K., N. Minagawa, M. Hyodo, T. Baba, T. Hori, and Y. Kaneda (2007), Effect of elastic inhomogeneity on the surface displacements in the northeastern Japan: Based on three-dimensional numerical modeling, *Earth Planets Space*, *59*, 1083–1093.
- Savage, J. C. (1983), A dislocation model of strain accumulation and release at a subduction zone, *J. Geophys. Res.*, *88*, 4984–4996, doi:10.1029/JB088iB06p04984.
- Savage, J. C. (1987), Effect of crustal layering upon dislocation modeling, *J. Geophys. Res.*, *92*, 10,595–10,600, doi:10.1029/JB092iB10p10595.
- Savage, J. C. (1998), Displacement field for an edge dislocation in a layered half-space, *J. Geophys. Res.*, *103*, 2439–2446, doi:10.1029/97JB02562.
- Simons, M., Y. Fialko, and L. Rivera (2002), Coseismic deformation from the 1999 M_w 7.1 Hector Mine, California, earthquake as inferred from InSAR and GPS observations, *Bull. Seismol. Soc. Am.*, *92*, 1390–1402, doi:10.1785/0120000933.
- Singh, S. J. (1970), Static deformation of a multilayered half-space by internal sources, *J. Geophys. Res.*, *75*, 3257–3263, doi:10.1029/JB075i017p03257.
- Subarya, C., M. Chlieh, L. Prawirodirdjo, J. P. Avouac, Y. Bock, K. Sieh, A. Meltzner, D. H. Natawidjaja, and R. McCaffrey (2006), Plate-boundary deformation associated



- with the great Sumatra-Andaman earthquake, *Nature*, 440, 46–51, doi:10.1038/nature04522.
- Turcotte, D. L., and G. J. Schubert (2002), *Geodynamics: Applications of Continuum Physics to Geological Problems*, 2nd ed., Cambridge Univ. Press, New York.
- Wald, D. J., and R. W. Graves (2001), Resolution analysis of finite fault source inversion using one- and three-dimensional Green's functions: 2. Combining seismic and geodetic data, *J. Geophys. Res.*, 106, 8767–8788, doi:10.1029/2000JB900435.
- Wei, W. B., et al. (2001), Detection of widespread fluids in the Tibetan crust by magnetotelluric studies, *Science*, 292, 716–719, doi:10.1126/science.1010580.
- Williams, C. A., and G. Wadge (1998), The effects of topography on magma chamber deformation models: Application to Mt Etna and radar interferometry, *Geophys. Res. Lett.*, 25, 1549–1552, doi:10.1029/98GL01136.
- Williams, C., M. Knepley, B. Aagaard, and S. Kientz (2007), PyLith: User manual, version 0.8.2, Comput. Infrastructure for Geodyn., Davis, Calif. [Available at http://www.geodynamics.org/cig/software/pylith/previous_releases.]
- Yu, S. B., et al. (2001), Preseismic deformation and coseismic displacements associated with the 1999 Chi-Chi, Taiwan, earthquake, *Bull. Seismol. Soc. Am.*, 91, 995–1012, doi:10.1785/0120000722.
- Zhao, D. P., K. Asamori, and H. Iwamori (2000), Seismic structure and magmatism of the young Kyushu subduction zone, *Geophys. Res. Lett.*, 27, 2057–2060, doi:10.1029/2000GL011512.